

Enhancing Expressivity of Quantum Neural Networks Based on the SWAP test

Sebastian Nagies,^{1,2,*} Emiliano Tolotti,³ Davide Pastorello,^{4,2} and Enrico Blanzieri^{3,2}

¹*Pitaevskii BEC Center and Department of Physics,*

University of Trento, Via Sommarive 14, 38123 Trento, Italy

²*INFN-TIFPA, Trento Institute for Fundamental Physics and Applications, Trento, Italy*

³*Department of Information Engineering and Computer Science,
University of Trento, Via Sommarive 9, 38123 Trento, Italy*

⁴*Department of Mathematics, Alma Mater Studiorum - University
of Bologna piazza di Porta San Donato 5, 40126 Bologna, Italy*

Parameterized quantum circuits represent promising architectures for machine learning applications, yet many lack clear connections to classical models, potentially limiting their ability to translate the wide success of classical neural networks to the quantum realm. We examine a specific type of quantum neural network (QNN) built exclusively from SWAP test circuits, and discuss its mathematical equivalence to a classical two-layer feedforward network with quadratic activation functions under amplitude encoding. Our analysis across classical real-world and synthetic datasets reveals that while this architecture can successfully learn many practical tasks, it exhibits fundamental expressivity limitations due to violating the universal approximation theorem, particularly failing on harder problems like the parity check function. To address this limitation, we introduce a circuit modification using generalized SWAP test circuits that effectively implements classical neural networks with product layers. This enhancement enables successful learning of parity check functions in arbitrary dimensions which we analytically argue to be impossible for the original architecture beyond two dimensions regardless of network size. Our results establish a framework for enhancing QNN expressivity through classical task analysis and demonstrate that our SWAP test-based architecture offers broad representational capacity, suggesting potential promise also for quantum learning tasks.

I. INTRODUCTION

Quantum machine learning (QML) is a rapidly growing field that develops quantum algorithms for machine learning tasks [1–5]. Quantum mechanics provides unique resources such as entanglement and nonstabilizerness that underlie potential quantum advantages over classical computation. QML algorithms can potentially outperform classical machine learning approaches by operating within this quantum framework, as demonstrated for example in the quantum support vector machine [6].

Quantum neural networks (QNNs) are a key component of QML, which aim to extend the success of classical neural networks to the quantum domain. QNNs are hybrid quantum-classical systems that adjust the training parameters of a parametrized quantum circuit through classical optimization of an objective function, based on measurements obtained after running the circuit [7, 8]. Broadly speaking, two main approaches to QNNs have been developed. The first and most widely adopted approach is based on variational quantum circuits (VQCs) [9], employing parametrized quantum circuits tailored specifically to the problem or the respective quantum hardware [10–12]. The most prominent example in this class is the Hardware Efficient Ansatz [13].

The second approach to QNNs is to design architectures that, in contrast to the first approach, resemble classical neural networks more closely. These schemes

generalize basic building blocks (e.g., perceptrons) to the quantum circuit setting [14, 15] and could hold the potential of transferring the impressive successes of classical neural networks to the quantum realm. In both cases, crucial limitations such as the barren plateau problem [16–18] must be addressed before these systems could become useful for real-world applications.

This paper focuses on QNN architectures based on the SWAP test quantum circuit [19–21] and addresses a specific limitation: their expressivity on classical datasets, which could potentially have implications for their performance on quantum learning tasks.

The SWAP test [22] measures the overlap between two arbitrary quantum states and is functionally equivalent to a classical perceptron with quadratic activation function when processing quantum states representing classical data via amplitude encoding [23], thus enabling construction of quantum perceptrons as QNN building blocks. The SWAP test quantum circuit can be implemented across various quantum computing platforms by decomposing it into platform-specific native gate sets, including superconducting qubits [11, 24, 25], trapped ions [26–29], and neutral atoms [30, 31]. Alternatively, the SWAP test can be directly implemented in experiment, as demonstrated with optical platforms [32–34] and trapped ions [35, 36]. Hence, the SWAP test is a suitable building block for near-term QNNs.

Pastorello and Blanzieri [21] proposed a two-layer feedforward neural network based on only SWAP test circuits as modules for quantum neural network construction. These modules execute SWAP tests between input and weight vectors using amplitude encoding to realize

* sebastian.nagies@unitn.it; Corresponding author

quadratic activation functions and can potentially be restricted to a small number of qubits. However, feedforward neural networks with only one hidden layer and quadratic activation functions do not satisfy the universal approximation theorem [37, 38] and would require deep architectures to approximate complex functions.

This work generalizes this modular QNN architecture to enable more expressive quantum neural networks. To this end we propose using generalized SWAP test circuits as building blocks: They can be implemented with multiple Fredkin gates controlled by a single shared ancilla qubit but acting on multiple sets of inputs and weights, effectively increasing the degree of the polynomial activation function. This new architecture can scale the degree of the activation function arbitrarily high, enhancing network expressivity as demonstrated through numerical experiments. Results show the architecture can approximate complex functions such as higher-dimensional parity checks that are impossible to learn with the original design. The architecture closely resembles classical polynomial neural networks [39, 40] or neural networks with product layers [41, 42].

This paper is organized as follows: Section II explains how QNNs can be constructed from SWAP tests and introduces a generalized quantum circuit architecture that effectively implements a product layer. Section III presents numerical results demonstrating our architecture’s performance on both classical real-world datasets and the challenging synthetic parity check function. Section IV validates the practical feasibility of our approach by running a pretrained model on real quantum hardware to learn the parity check function. Section V summarizes our findings and conclusions.

II. CONSTRUCTING QUANTUM NEURAL NETWORKS WITH SWAP TESTS

The quantum SWAP test is a fundamental operation in quantum computing which allows for the estimation of the overlap between two arbitrary quantum states. When representing classical vectors with those quantum states via amplitude encoding, the output of the SWAP test is functionally equivalent to the output of a classical perceptron used in feedforward neural networks. Whereas many parametrized quantum circuits have little resemblance to classical neural networks, a quantum neural network composed of SWAP test circuits as its building blocks has a one-to-one correspondence with its classical counterparts [21]. Given the extraordinary success of classical neural networks for machine learning tasks, this QNN architecture potentially holds great promise for quantum learning applications as well.

This section provides a brief review of the SWAP test quantum circuit and demonstrates how quantum feedforward neural networks can be constructed from these building blocks. We discuss the universality of this architecture and introduce a simple generalization in Section

IID that significantly enhances expressivity on certain classical datasets (see Section III). At the end, we comment on the architecture’s scalability on current quantum hardware in Section II E.

A. SWAP test

Given two quantum states $|\psi\rangle$ and $|\phi\rangle$, the SWAP test circuit operates as follows (see Fig. 1):

1. Initialize an ancilla qubit in the $|0\rangle$ state.
2. Apply a Hadamard gate to the ancilla qubit.
3. Apply a controlled-SWAP operation, with the ancilla qubit as the control and $|\psi\rangle$ and $|\phi\rangle$ as the targets.
4. Apply another Hadamard gate to the ancilla qubit.
5. Measure the ancilla qubit in the computational basis.

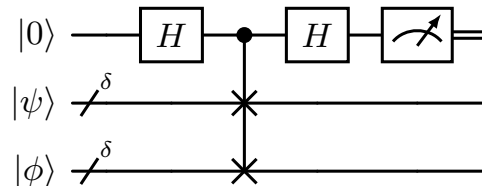


Figure 1. Quantum circuit implementing the SWAP test which estimates the overlap between two quantum states $|\psi\rangle$ and $|\phi\rangle$ by measuring an ancilla qubit initialized to state $|0\rangle$. Both states are represented on quantum registers with δ qubits. If the two quantum states encode classical inputs and weights via amplitude encoding in a quantum perceptron context, the number of required qubits is $\delta = \lceil \log_2 d \rceil$, where d is the dimension of the classical input and weights vectors.

The probability P of measuring the ancilla qubit in the $|0\rangle$ state is then given by:

$$P(0) = \frac{1}{2}(1 + |\langle\psi|\phi\rangle|^2) \quad (1)$$

This probability is directly related to the overlap between the two input states: For two orthogonal (identical) states the probability is $P(0) = 0.5$ ($P(0) = 1$). Through repeated preparation of the input states and measurement of the ancilla qubit after the SWAP test, this probability (and thus the overlap between the two states) can be estimated to arbitrary precision ϵ with $\mathcal{O}(\epsilon^{-2})$ samples.

On certain quantum computing platforms, such as photonic or trapped ion quantum computers, the SWAP test can be implemented natively [32–36], thus making it an attractive building block for quantum machine learning applications. On other platforms (e.g. superconducting qubits) the SWAP test needs to be decomposed into the respective native gate set first.

B. Quantum perceptron

A classical perceptron typically takes as input a classical d -dimensional vector \mathbf{x} , is parametrized by a d -dimensional weight vector \mathbf{w} and a bias b , and outputs a single number $m(\mathbf{x}; \mathbf{w}, b)$. The whole procedure can be written as

$$m(\mathbf{x}; \mathbf{w}, b) = \sigma(\mathbf{x} \cdot \mathbf{w} + b), \quad (2)$$

where \cdot denotes the dot product and σ is a nonlinear activation function. Common choices for σ include non-polynomial functions like the sigmoid or ReLU. However, polynomial activation functions, particularly quadratic ones ($\sigma(z) = z^2$), have also been investigated [39, 43] and are relevant to the quantum setting discussed in this work.

Comparing with Eq. 1, we can observe that the output of the SWAP test is formally similar to that of a classical perceptron. Specifically, the overlap $|\langle \psi | \phi \rangle|^2$ can be identified with a classical cosine similarity pre-activation paired with a quadratic activation function.

Cosine similarity is sometimes used in classical perceptrons as an alternative to the simple dot product, as it provides a bounded pre-activation value between -1 and 1 and achieves better performance in certain contexts [44]:

$$\cos(\mathbf{x}, \mathbf{w}) = \frac{\mathbf{x} \cdot \mathbf{w}}{\|\mathbf{x}\| \cdot \|\mathbf{w}\|}. \quad (3)$$

To establish the link to the inner product of quantum states $\langle \psi | \phi \rangle$, we first encode a d -dimensional classical input \mathbf{x} into the quantum state $|\psi\rangle$ via amplitude encoding [23] as follows:

$$|\psi\rangle = \frac{1}{\|\mathbf{x}\|} \sum_{i=1}^{2^\delta} x_i |i\rangle, \quad (4)$$

where we need $\delta = \lceil \log_2 d \rceil$ qubits for the encoding and $|i\rangle$ are the computational basis states. After encoding the weights \mathbf{w} analogously, one easily sees that the inner product of the quantum states is equivalent to the classical cosine similarity.

To make the correspondence to the classical case complete, one would also need a bias parameter which offsets the result of the inner product before passing it to the activation function (squaring it in this case). Although we can not implement this directly with the here considered architecture, we can achieve something similar by introducing a dummy input feature: Instead of a d -dimensional input \mathbf{x} , we use a $(d+1)$ -dimensional input \mathbf{x}' , where we always set the last feature to 1. The last parameter w_{d+1} of the $(d+1)$ -dimensional weight vector \mathbf{w}' then acts as an effective bias and the output of the SWAP test (again assuming amplitude encoding) is given by

$$P(0) = \frac{1}{2} \left(1 + \left| \frac{\mathbf{x} \cdot \mathbf{w} + w_{d+1}}{\|\mathbf{x}'\| \cdot \|\mathbf{w}'\|} \right|^2 \right). \quad (5)$$

Note that this is not completely equivalent to the classical perceptron (Eq. 2), as the bias in this case is included in \mathbf{w}' and is thus part of the pre-activation function ($\|\mathbf{x}'\| = \sqrt{\|\mathbf{x}\|^2 + 1}$ and $\|\mathbf{w}'\| = \sqrt{\|\mathbf{w}\|^2 + w_{d+1}^2}$). Nevertheless, as our numerical results in Sec. III show, this architecture is still suitable to learn classical datasets.

C. Two-layer feedforward neural network

Similarly to classical neural networks, quantum perceptrons based on SWAP tests can be combined to form a feedforward neural network. We consider a two-layer quantum-classical hybrid architecture for binary classification tasks, where the network's output is computed as:

$$\begin{aligned} f(\mathbf{x}; \{\mathbf{w}\}) &= \sum_{i=1}^N c_i P_i(0) + b \\ &= \sum_{i=1}^N \frac{c_i}{2} (1 + |\langle \mathbf{x}' | \mathbf{w}'_i \rangle|^2) + b. \end{aligned} \quad (6)$$

Here, the classical d -dimensional input vector \mathbf{x} is encoded into a quantum state $|\mathbf{x}'\rangle$ via amplitude encoding (Eq. 4). The prime denotes again that the input contains a dummy feature to realize a bias term (see previous section). The state $|\mathbf{x}'\rangle$ serves as the input to N distinct SWAP tests in the first layer. Each SWAP test i utilizes a unique classical weight vector \mathbf{w}_i as well as a bias, both of which are encoded together into the quantum state $|\mathbf{w}'_i\rangle$. In the rest of the article we will drop the prime notation and always assume that the input contains an additional dummy feature and one of the weights acts as a bias.

The N SWAP tests can be executed in parallel. Alternatively, they can be performed sequentially on the same quantum circuit, requiring repeated initialization of the weight and input states for each test. The first layer's outputs are the N probabilities, $P_i(0)$, obtained from measuring the ancilla qubit of each SWAP test in the state $|0\rangle$.

In the second, purely classical layer, these N probabilities are multiplied by their respective coefficients c_i and then summed to produce a single scalar output. Finally we also add a classical bias b in the second layer, which can be convenient for shifting the output of the network to fit with a chosen loss function. Overall, the network has $N(d+2) + 1$ trainable parameters, consisting of Nd weights (from the N d -dimensional vectors \mathbf{w}_i), N biases

in the quantum layer, N classical coefficients c_i and a single classical bias in the second layer.

Crucially, this network architecture does not satisfy the universal approximation theorem (UAT). The standard UAT typically requires non-polynomial activation functions [38, 45], whereas the activation function implicit in $|\langle \mathbf{x} | \mathbf{w}_i \rangle|^2$ is polynomial (quadratic) in the components of \mathbf{x} and \mathbf{w}_i . Furthermore, as discussed in the last section, the way we implement the bias is not equivalent to a bias term in a classical perceptron. In Sec. III, we will empirically demonstrate that this architecture is nevertheless suitable for learning many real-world datasets. However, as shown with the parity check example in Sec. III, certain challenging classical functions are impossible for this neural network to learn. Successfully learning such functions necessitates modifications to the quantum architecture. Several proposals exist in the literature for realizing non-polynomial activation functions (e.g., sigmoid) on quantum hardware [14, 15, 46]. However, in the next section we will introduce a simple modification to the current quantum neural network which allows us to stick with the SWAP test based architecture and is designed to enable the learning of these more challenging classical functions.

D. Constructing a product layer

The major drawback of the two-layer feedforward quantum neural network architecture discussed in the previous section is the quadratic activation function which limits the networks capability to learn certain classical datasets like the parity check. However, we can slightly modify the original SWAP test quantum circuit in order to increase the degree of the polynomial activation function to arbitrary even degrees.

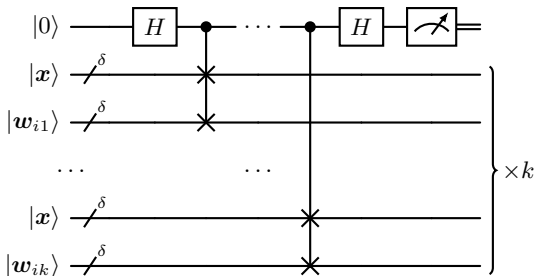


Figure 2. Generalization of the SWAP test to a product module. w_{ij} is the weight vector in product module i , with factor index j . $\delta = \lceil \log_2(d+1) \rceil$ is the number of qubits needed to encode the input and weight vectors \mathbf{x} and \mathbf{w}_{ij} of dimension d and $d+1$ respectively (assuming one of the weights acts as a bias). The overall product module can be seen as a number of k SWAP tests (see Fig. 1) being executed using the same ancilla qubit. After measuring said ancilla, the probability $P(0)_i$ corresponds to a polynomial activation function of degree $2k$ (see Eq. 7).

Our proposed generalization of the SWAP test is depicted in Fig. 2. Whereas in the original SWAP test (see Fig. 1) the circuit was composed of one copy of input state $|\mathbf{x}\rangle$ and weights $|\mathbf{w}\rangle$ as well as a single ancilla qubit, here we consider a number of k copies of the input state as well as k (generally different) states $|\mathbf{w}_{ij}\rangle$. The difference now lies in the fact that all k pairs of inputs and weights (which we refer to as *factor modules*) share the same single ancilla qubit (again initialized to $|0\rangle$), i.e. we perform k SWAP tests using the same ancilla qubit before measuring its probability $P(0)_i$. Analogous to the standard setup (Eq. 6), we have N different instances of these *product modules*. Note that these product modules can be equivalently thought of as regular SWAP tests using a generalized amplitude encoding, where multiple copies of the classical input state are encoded into the quantum register.

In the second layer the output probabilities get again multiplied by classical coefficients c_i and summed up. The overall output of this generalized two-layer neural network (the first layer is a quantum version of a *product layer*, requiring N measurements, while the second layer is purely classical), can be computed as

$$f(\mathbf{x}; \{\mathbf{w}\}) = \sum_{i=1}^N c_i P(0)_i + b = \sum_{i=1}^N \frac{c_i}{2} \left(1 + \prod_{j=1}^k |\langle \mathbf{x} | \mathbf{w}_{ij} \rangle|^2 \right) + b. \quad (7)$$

Here we have a total of N classical coefficients c_i , a single classical bias b , Nk biases and Nkd weights in the quantum layer, for an overall number of $N[k(d+1)+1]+1$ trainable parameters.

For $k=1$ this modified neural network architecture recovers the original two-layer feedforward network discussed in Sec. II C. Note that for $k>1$, we have two possibilities: First, all the weight vectors $|\mathbf{w}_{ij}\rangle$ for a given product module with index i can be chosen equal. In this case the network is equal to the standard two-layer feedforward network architecture in Eq. 6, but with an activation function of degree $2k$ instead of quadratic. However, we can also allow the weight vectors to be different from each other within the same product module, in which case the network has a similar structure to so called sigma-pi-sigma networks [41, 42].

Formally, the new neural network architecture still does not satisfy the universal approximation theorem, as the activation function remains polynomial. However, as we can increase the (even) degree of the activation function arbitrarily by increasing k , one can reasonably hope that this will become irrelevant for large networks and real-world datasets. Furthermore, for more general classical networks of sigma-pi-sigma type, there are universal approximation results which don't require a non-polynomial activation function [47, 48]. As our architecture is not fully equivalent to those classical neural

networks, we leave it for future work to give a more rigorous analysis of the universality of our quantum neural network.

Nevertheless, in Sec. III and Appendix C we will give numerical evidence (using the parity check and the n -spiral task) which lets us conjecture that, by increasing the number of product modules as well as the number k of factor modules contained within each of them, the proposed architecture can indeed learn certain hard classical datasets in arbitrary dimensions.

E. Scalability of the quantum neural network

A key bottleneck when implementing the proposed quantum neural network architectures on quantum hardware is the number of available qubits for currently realizable quantum SWAP tests. Some classical datasets (and similar considerations apply to quantum data) have a large dimension d , e.g., image classification problems. In those cases, potentially there aren't enough available qubits to encode the whole vector into a single quantum state. In [21] the authors explain how in such cases the input can be split onto multiple SWAP test modules. For the original quantum neural network (without product layers, see Sec. II) the output of the network is then modified to

$$f(\mathbf{x}; \{\mathbf{w}\}) = \sum_{i=1}^N \frac{c_i}{2} \left(1 + |\langle \mathbf{x}^{(i)} | \mathbf{w}_i \rangle|^2 \right) + b, \quad (8)$$

where $\mathbf{x}^{(i)}$ amplitude encodes now only a subset of the features in the original input vector \mathbf{x} . The subset of features each different SWAP test receives can be varied for each module. Furthermore the subsets are also allowed to overlap or repeat across modules. This strategy can of course be equally applied to the modified network with product layers discussed in Sec. IID. In this case, the input features can also be split across the k factor modules within each product module, instead of giving each factor module the same input, which allows for further generalization of the QNN architecture.

In Appendix A we demonstrate with the example of the MNIST dataset [49] that the quantum neural network architecture defined in Eq. 7 can reliably learn higher-dimensional input data, even when the features are split into multiple generalized SWAP tests.

III. ASSESSING EXPRESSIVITY ON CLASSICAL DATASETS

In this section we demonstrate the capability of our proposed quantum neural network architecture, based on the generalized SWAP test circuit (see Sec. IID), to learn classical datasets. This expressivity for classical learning tasks can potentially be important if one hopes

to translate the impressive applications and successes of neural networks to quantum learning tasks.

We start in Subsec. III A with explaining our numerical implementation of the architecture and the metrics we use for quantifying its expressivity. We then train the network on 21 different real-world data sets in Subsec. IIIB, before moving to the harder to learn parity check function in Subsec. IIIC. Here we give an analytical argument for why the original two-layer network (without product layer) can never learn the higher-dimensional parity check and then present our numerical results for the generalized architecture, which strongly suggest that our proposed modified architecture can learn the function in arbitrarily high dimensions.

In the Appendices A and C we extend our numerical analysis to two more examples: The MNIST handwritten digits dataset, which has a high input dimension where features can be split onto multiple modules, as well as the two-dimensional spiral classification task, which is usually hard to learn for neural networks (similar to the parity check). These examples further demonstrate the advantage in expressivity of our proposed QNN architecture with a product layer.

A. Implementation and training

In a possible experimental implementation of the quantum neural network architecture proposed in the last section, the first layer of the network would be run on a quantum computer (initializing input, executing SWAP tests, measurement of ancilla qubits), while the second layer is computed classically. For most of this work we simulate the entire process purely classically (which is feasible for the considered classical datasets and network sizes), i.e., the output probabilities after the first quantum layer (either the standard version or with product layers, see Eqs. 6 and 7) are computed exactly instead of sampling them from repeated real measurements. The only exception to this occurs in Sec. IV, where we run a pretrained product layer quantum neural network on real quantum hardware.

For training the neural networks, we implemented a classical surrogate of the QNN in Python with the PyTorch library, which allows us to effectively implement and extensively test the product layer on a GPU. The surrogate outputs the same probabilities as the quantum circuit. Specifically, we implemented the single hidden-layer QNN defined in Eq. 7, with the difference that we rescaled the output probabilities to be in the range $[0, 1]$ for convenience, i.e. the PyTorch QNN output is defined as

$$f(\mathbf{x}; \{\mathbf{w}\}) = \sum_{i=1}^N c_i (2P(0)_i - 1) + b, \quad (9)$$

where $P(0)_i$ is the probability of measuring 0 in the ancilla qubit for the i -th product module (Eq. 7), and c_i

Dataset	Samples	Features
01_iris_setosa_versicolor	50/50	4
01_iris_setosa_virginica	50/50	4
01_iris_versicolor_virginica	50/50	4
03_vertebral_column_2C	100/210	6
04_seeds_1_2	70/70	7
05_ecoli_cp_im	77/143	7
06_glasses_1_2	42/38	9
07_breast_tissue_adi_fadmasgla	49/22	9
08_breast_cancer	44/36	9
09_accent_recognition_uk_us	63/17	12
10_leaf_11_9	14/16	14
11_banknote_authentication	610/762	4
12_transfusion	178/570	4
13_diabetes	268/500	8
14_haberman_survival	225/81	3
15_indian_liver_patient	416/167	10
16_ionosphere	225/126	34
17_wdbc	357/212	30
18_wine_quality_red_5	855/744	11
19_wine_quality_white_5	3258/1640	11
20_rice_cammeo_osmancik	1630/2180	7

Table I. UCI datasets used for the numerical tests.

are the coefficients in the linear combination of modules. The trainable parameters are initialized randomly with a standard normal distribution, and the training is performed using the Adam optimizer. As a loss function, we considered the binary cross-entropy with logits (log-loss with a sigmoid activation), which is well-suited for binary classification tasks.

For the numerical tests, the training is performed with no mini-batch and a learning rate of $\eta = 1$. We considered 50000 epochs and early stopping with 5000 epochs patience on the validation set F1 score. We utilized a 10-fold cross-validation method, and split each training set into 80% training and 20% validation sets.

To evaluate the performance of the architecture, we consider accuracy as well as the F1 score, since the latter is a more robust metric for unbalanced datasets. The accuracy is defined as the ratio between the number of correctly classified samples over the total number of test samples. The F1 score is defined as the harmonic mean of precision and recall.

B. Learning real-world data sets

To test the general capabilities of our architecture (Eq. 7), we use the network as a binary classifier and learn different real-world classical datasets, originally from the UCI machine learning repository [50]. The considered 21 datasets are reported in Table I, and some of them have been preprocessed to be suitable for binary classification.

We carried out numerical tests with the PyTorch implementation of our proposed QNN architecture, for different combinations of the number of product modules $N \in \{1, 3, 5, 10\}$ and factor modules $k \in \{1, 2, 3\}$ in the

product layer. The results are shown in Fig. 3, where we report the accuracy and F1 score on the respective test set for all datasets. We can see that the architecture is able to learn the majority of the considered datasets, with good values of accuracy and F1 score.

Moreover, we note a slight positive scaling in the prediction performance for the number of product modules N , especially pronounced when passing from a single module to multiple modules. This is expected, as the expressivity of the network increases with the number of modules, and the larger number of modules can represent the same functions as a smaller number of modules. However, the number of factor modules k in the product layer does not seem to have a noticeable impact on the performance, as we find similar results for different k , suggesting that with these real world datasets the original architecture (Eq. 6) is sufficient. The same trend is also observed for individual datasets, where we find that the performance is similar for different values of k .

The outliers in the F1 score boxplot are related to the transfusion dataset achieving an F1 score around 0.4, which is significantly below the scores observed for other datasets. However, this dataset has high class imbalance and correlation between two of the four features.

For more complex datasets, such as the IJCNN1 dataset [51], we find that the product layer increases the prediction performance. We merged the original training and test sets into a single dataset containing 22 features and 61615 samples, to utilize the same 10-fold cross-validation procedure as above. Specifically, in Fig. 4 we show the F1 score for the IJCNN1 dataset, for different combinations of product modules N and factor modules k in the product layer, obtained with the PyTorch implementation utilizing the same training and testing procedure as above, with the same parameters. We considered the F1 score as the only performance metric, since the dataset is heavily unbalanced (with $\sim 90\%$ of the samples belonging to one of the two classes). We can see that the product layer is able to increase the F1 score, and the performance increases with the number of product modules N and factors k in the product layer, needing more than one factor to cross the 0.9 mean F1 score threshold.

C. Learning high-dimensional parity checks

While the last section showed a vast number of real-world datasets which can be easily learned by the standard two-layer feedforward architecture of the SWAP test-based QNN (introduced in Subsec. IIC), we discuss in this section the parity check function, which is well known to be hard to learn for many types of neural networks [52]. Indeed, we present in Subsec. IIIC 1 an analytical argument for why the quadratic activation function, used in the SWAP test-based architecture, prohibits the standard two-layer feedforward network to learn, even in principle, the d -dimensional parity check function, for $d > 2$. In Subsec. IIIC 2 we

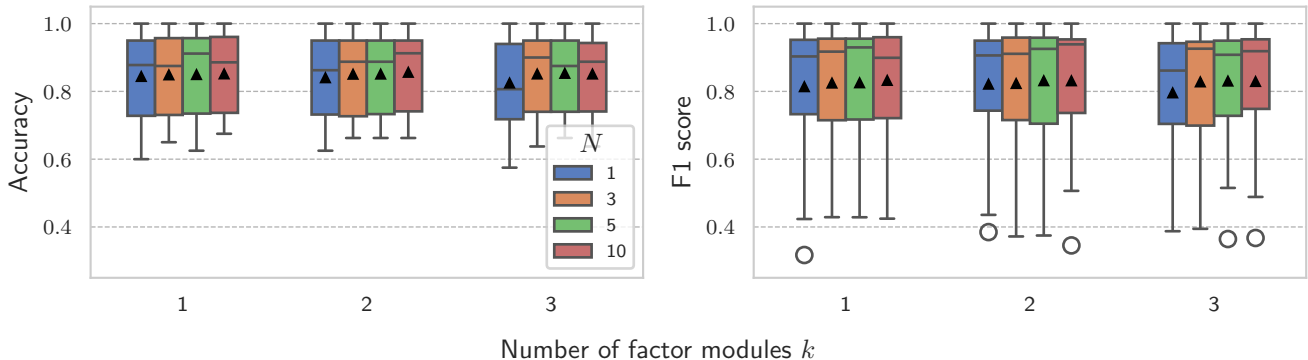


Figure 3. Accuracy and F1 score distribution on the real-world datasets with the PyTorch implementation of the QNN with product layer (see Eq. 7), for increasing number of product modules N and factor modules k . Each boxplot contains 21 points, each one being the mean value across different folds for each dataset (see Sec. III A). Horizontal lines represent the median for all datasets and triangle markers indicate mean values.

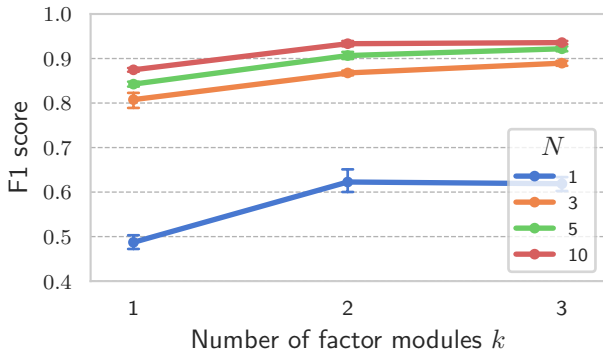


Figure 4. F1 scores for learning the IJCNN1 dataset with our QNN architecture (Eq. 7). Points represent mean values across different folds, and error bars represent 95% confidence intervals.

then demonstrate with numerical experiments that our proposed modification of the original architecture with product layers (see Subsec. IID) allows us to enhance the expressivity of the original network and learn the parity check in arbitrary dimensions. In Appendix C we repeat a similar numerical analysis for another hard-to-learn function: the n-spiral task, for which we find a similar increase in expressivity when using the generalized quantum neural network with product layers.

1. Limited expressivity of the QNN without product layer

A standard classical two-layer NN with quadratic activation functions does not satisfy the universal approximation theorem [38, 45]. The original quantum neural network architecture (without a product layer), defined in Eq. 6, differs slightly from its classical counterpart,

as the bias is encoded in an additional weight parameter (see also discussion in Sec. IIB). It is thus a priori not clear if the universal approximation theorem equally applies to this QNN for learning classical datasets. However, even if the universal approximation property does not apply, the network can still be suitable for many real-world learning tasks as shown in the previous section.

In this section we give a simple analytical argument for why the standard two-layer feedforward quantum neural network (Eq. 6) will indeed always fail at some learning tasks, even for small input dimensions. Specifically, we show that the d -dimensional parity check function (with $d > 2$) can never be fully learned due to the quadratic activation function inherent to the SWAP test based architecture. We note that similar results on the limited expressivity of QNN's for the parity check function have been previously discussed in Ref. [53].

We define the d -dimensional parity check function f_{PC} taking as input a d -dimensional real vector \mathbf{x} with non-zero entries and outputs $f_{PC}(\mathbf{x}) = \text{sgn}\left(\prod_{i=1}^d x_i\right)$, i.e. if x has an even number of negative entries the function output is $+1$, otherwise -1 . The d -dimensional Euclidean space can be separated into the different odd or even orthants. We denote any vector in an even orthant as \mathbf{x}^+ , for which $f_{PC}(\mathbf{x}^+) = +1$ holds. Correspondingly we define $f_{PC}(\mathbf{x}^-) = -1$ for vectors \mathbf{x}^- in odd orthants. Examples for \mathbf{x}^+ in two dimensions are $(1, 1)$ and $(-1, -1)$.

In our analysis we restrict ourselves, without loss of generality, to only the 2^d vectors $\{\pm 1\}^d$, one in each orthant. We label all these representative vectors as \mathbf{x}_i^+ and \mathbf{x}_i^- , with $i = 1, \dots, 2^d/2$. The task is then to show that the two-layer feedforward neural network with quadratic activation functions (Eq. 6) is not able to correctly label all 2^d of these vectors.

A necessary requirement for the neural network to correctly label all the representative vectors is

$$f(\mathbf{x}_i^+) > f(\mathbf{x}_i^-), \quad \forall i, j, \quad (10)$$

i.e. there has to be some threshold value for the output of the neural network, that correctly distinguishes between the two classes \mathbf{x}^+ and \mathbf{x}^- . The condition $f(\mathbf{x}_i^+) < f(\mathbf{x}_i^-)$ is equivalent and can be obtained by simply flipping the signs of all classical coefficients c_i in Eq. 6. The condition above furthermore also implies

$$\sum_i f(\mathbf{x}_i^+) > \sum_i f(\mathbf{x}_i^-), \quad (11)$$

where the sums run over all $2^d/2$ representative vectors in the respective orthants with label +1 or -1. After inserting the definition of the neural network output f (Eq. 6) and explicitly writing out the bias as the $(d+1)$ st entry $w_{j,d+1}$ of the weight vector \mathbf{w}_j (Eq. 5), we get the following condition:

$$\sum_i \sum_{j=1}^N c_j \frac{(\mathbf{x}_i^+ \cdot \mathbf{w}_j + w_{j,d+1})^2 - (\mathbf{x}_i^- \cdot \mathbf{w}_j + w_{j,d+1})^2}{\|\mathbf{x}'\|^2 \|\mathbf{w}'_j\|^2} > 0, \quad (12)$$

where we used the fact that $\|\mathbf{x}'\| \equiv \sqrt{\|\mathbf{x}_i^\pm\|^2 + 1}$ is the same for all 2^d representative vectors we consider. Using the following identity for $d \geq 3$ (see Appendix B for the derivation):

$$\sum_i (\mathbf{x}_i^\pm \cdot \mathbf{w}_j)^2 = 2^{d-1} \|\mathbf{w}_j\|^2, \quad (13)$$

we can further simplify our condition to

$$\sum_{j=1}^N \frac{c_j w_{j,d+1}}{\|\mathbf{w}'_j\|^2} \mathbf{w}_j \cdot \sum_i (\mathbf{x}_i^+ - \mathbf{x}_i^-) > 0. \quad (14)$$

We now note that $\sum_i \mathbf{x}_i^+ = \sum_i \mathbf{x}_i^- = 0$. This can be easily seen from symmetry or by specifically considering an arbitrary entry in \mathbf{x}_i^\pm : If that entry is +1, there are 2^{d-2} possible configurations of signs in the remaining entries, so that the vector lies in an orthant with label \pm . Analogously there are 2^{d-2} other vectors with label \pm where that specific entry is -1. In the sum over all vectors \mathbf{x}_i^\pm this entry will then cancel to zero. The same argument holds for all other entries in \mathbf{x}_i^\pm .

We thus find that the left side of Eq. 14 evaluates to zero and the inequality can never be fulfilled (in Appendix B we show the corresponding condition for $d = 2$, which can be fulfilled). From this we conclude that the set of representative vectors can never be distinguished by the two-layer feedforward neural network architecture for $d \geq 3$. Note that the above argument equally applies when the representative set is rotated or rescaled

arbitrarily. As those representative vectors are a subset of possible inputs in the d -dimensional parity check, the function can also not be learned in the general case. This argument is independent of the chosen weights, biases and number of modules in the network. We emphasize that this is a fundamental limitation of the architecture due to the quadratic activation function (which also holds for the analogous classical network with biases not encoded in the weights vectors).

Our numerics in the following section confirm this argument: We find the parity check for $d = 2$ to be easily learnable but impossible for $d \geq 3$. However, we numerically show that our in Subsec. IID proposed generalization of the SWAP test-based quantum neural network can overcome this limitation and learn the parity check function in arbitrary dimensions.

2. Numerical results

We carried out numerical tests on the parity check data set, with the PyTorch implementation (see Sec. III A), considering input dimensions from 1 to 10. We considered the generalized architecture define in Eq. 7, with product modules with repeated inputs for each factor module and a bias encoded in the weights (see Sec. IIB). We generated synthetic data sets of the d -dimensional parity check function in a balanced manner, considering s uniformly distributed samples $\in U[0, 1]$ in each of the 2^d different decision regions of the d -dimensional hypercube, represented by the different combinations of feature signs. In this sense, a d -dimensional parity check dataset contains $s \cdot 2^d$ samples. We generated training and test sets independently, with s and $0.2 \cdot s$ samples per region respectively.

From the numerical tests we find that the generalized QNN can classify the parity check dataset at least up to $d = 10$ by simultaneously increasing the number N of product modules and the number k of respective factor modules. We tested for multiple parity check input dimensions d , with different numbers of k factor modules and N product modules. In each case we randomly generated $s = 1000$ samples in each decision region.

Accuracy is considered as the maximum accuracy obtained on the test set, during 50000 epochs runs with no early stopping, considering different learning rates in the range $[0.01, 0.1, 1, 10]$. We considered a batch size of 256000 samples (due to GPU memory limit), since we observed sensitivity to the gradient calculation. Hence the training set is processed in a single batch for the gradient calculation at each epoch, except for the $N = 1000$ case for $d = 9, 10$, where we perform 2, 4 optimization steps per epoch respectively.

The achieved accuracies are shown in Fig. 5. From these results we can see that the generalized QNN architecture with a product layer can learn the parity check data set for all the considered dimensions to high accuracy, by increasing the number of factor modules k in

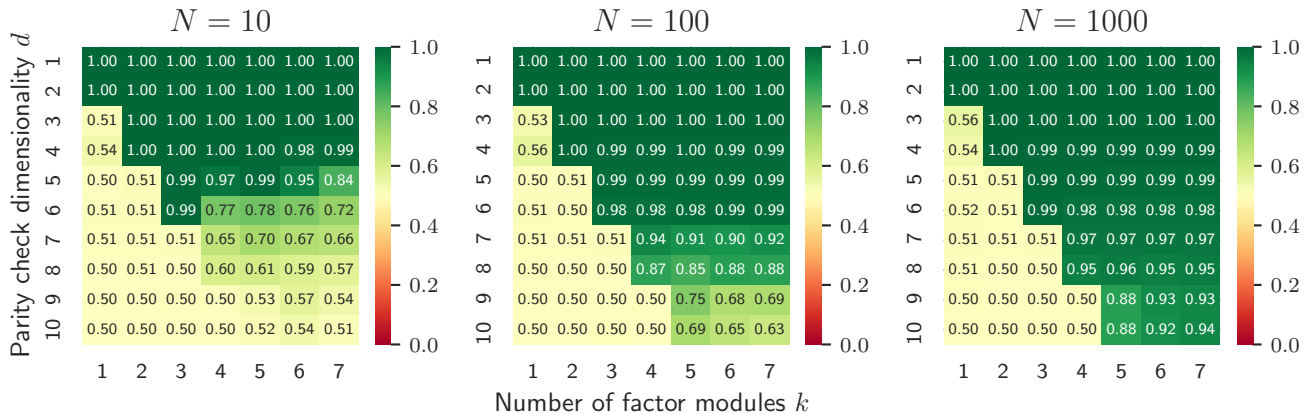


Figure 5. Accuracy results for the parity check data set with the PyTorch implementation of the product layer. d is the dimension of the parity check data set, k is the number of factors in the product layer and N is the number of modules. We generated 1000 samples in each of the 2^d respective decision regions. Each accuracy point is the maximum achieved accuracy on the test set, obtained by training the network for 50000 epochs, for learning rates in $[0.01, 0.1, 1, 10]$.

the product layer to be $k \geq \lceil d/2 \rceil$. The number of modules N is also important, as we find accuracy saturation for limited N . Finally, also the number of samples s is important for training, as it impacts accuracy at higher dimensions with increased problem difficulty. Specifically we found accuracy degradation for $s \leq 100$ samples per region, highlighting the sensitivity to gradient calculation for the training and the need for larger training sets.

The factor modules within each product module effectively realize a polynomial activation function of degree $2k$, which is consistent with the results about the limited expressivity of the parity check function for $d > 2$, discussed in the previous section, which only holds for quadratic activation functions.

IV. IMPLEMENTATION ON QUANTUM HARDWARE

To test the performance of our proposed quantum neural network architecture (see Eq. 7) under noisy conditions, we implemented it on real quantum hardware. Specifically, we tested the representation capability of the QNN for the three-dimensional parity check function with $N = 4$ product modules and $k = 2$ factor modules. We trained it purely classically, implemented it with the Qiskit library [54] and then ran the network with the learned weights on the *ibm_torino* QPU with a *Heron r1* processor. For comparison we also performed noiseless simulations of the circuit with the Qiskit Aer simulator.

The transpiled circuit for each of the $N = 4$ product modules, including the classical data amplitude encoding and SWAP test, averages a size of ≈ 277 gates (with ≈ 56 CZ gates), and an average circuit depth of ≈ 144 . The transpilation of the SWAP test circuit only, requires on average ≈ 183 gates (with ≈ 42 CZ gates) and a

circuit depth of ≈ 119 , while the amplitude encoding of the input data required on average ≈ 58 gates (with 4 CZ gates, one for each 2-qubit data register) and a circuit depth of 9. The difference between the sum of encoding and SWAP test circuit, and the total circuit is due to the additional gates required for qubit routing and topology constraints. Notably, the single Fredkin gate (CSWAP) requires 41 gates (with 10 CZ gates) and a depth of 35, which highlights the advantage of a native SWAP test hardware implementation.

We used the same accuracy definition as for the classical surrogate (see Sec. III A), and calculated the accuracy on the test set. The network achieved an accuracy of 100% on the test set for the classical surrogate (see Fig. 5), and 95% on the quantum circuit with the noiseless Aer simulator with 8192 shots. When running the circuit on the real QPU, we still achieved an accuracy of 84% with 8192 shots. Despite the slightly worse results on the real QPU due to hardware noise, the architecture was still able to exhibit high performance and classify the three-dimensional parity check data set with relatively high accuracy.

It should be noted that in the original paper (see Ref. [21]) on the QNN architecture defined in Eq. 6, the authors proposed a measurement protocol that performs the linear combination of modules by controlling the number of effective measurements for the i -th module to be proportional to c_i . For simplicity we utilized the same number of measurement shots for each module instead, and combined each output with the related c_i weight. There is thus potential for further increasing the accuracy when running the QNN on real quantum hardware.

V. CONCLUSIONS

To summarize, this work presents a comprehensive numerical study of the expressivity of quantum neural networks (QNN) based on the SWAP test quantum circuit across diverse classical datasets. We reviewed the mathematical equivalence between the QNN architecture and classical two-layer feedforward networks with quadratic activation functions under amplitude encoding (established in Ref. [21]). We then pointed out fundamental limitations stemming from the violation of the universal approximation theorem for polynomial activation functions.

To address these expressivity constraints, we introduced a modified QNN architecture that incorporates generalized SWAP test circuits as building blocks, effectively implementing a classical neural network with a product layer. This enhancement preserves the conceptually simple structure of the QNN, suitable for implementation on current hardware, while significantly expanding the network’s representational capacity for classical datasets.

Our extensive evaluation encompassed both real-world datasets (e.g. IRIS and MNIST) and challenging synthetic benchmarks like the parity check function. The results demonstrate a clear performance dichotomy: while the original QNN architecture successfully represents many real-world datasets, the product layer generalization proves essential for learning the more complex synthetic functions that expose fundamental expressivity limitations.

To further underline these limitations, we provided an analytical argument demonstrating that the original architecture fundamentally cannot learn parity check functions beyond two dimensions, regardless of network size. In contrast, for our generalized architecture with product layers, we gave compelling numerical evidence that it exhibits scalable learning capability, successfully classifying parity check problems in arbitrary dimensions.

The practical viability of our approach was validated through a quantum hardware implementation of a classically pretrained QNN with product layer, achieving 84% classification accuracy on three-dimensional parity check data despite the inherent noise on current quantum hardware. Our analysis of SWAP test compilation costs highlights the potential advantages of quantum platforms with direct SWAP test implementations, e.g. on optical platforms, for efficient deployment of these architectures.

Whether or not there are advantages of QNN’s modeled after classical neural networks compared to standard parametrized quantum circuits is not clear [55]. Nevertheless, the strong performance of our QNN architecture on classical learning tasks still raises compelling questions about its potential in quantum learning applications, e.g. quantum phase classification. Furthermore, this work leverages a framework for enhancing QNN expressivity through classical task analysis, an approach that could inform similar studies across other QNN architectures.

ACKNOWLEDGMENTS

We thank Stefano Azzini and Philipp Hauke for useful discussions. The authors are solely responsible for the content of this publication. S.N. acknowledges funding by the German Federal Ministry for Education and Research under the funding reference number 13N16437. E.T. was supported by the MUR National Recovery and Resilience Plan (PNRR) M4C1I4.1, funded by the European Union under NextGenerationEU. D.P. was supported by project SERICS (PE00000014) under the MUR National Recovery and Resilience Plan funded by the European Union – NextGenerationEU. D.P. is a member of the “Gruppo Nazionale per la Fisica Matematica (GNFM)” of the “Istituto Nazionale di Alta Matematica “Francesco Severi” (INdAM)”. Views and opinions expressed are however those of the author(s) only and do not necessarily reflect those of the European Union or The European Research Executive Agency. Neither the European Union nor the granting authority can be held responsible for them. This work has benefited from Q@TN, the joint lab between University of Trento, FBK—Fondazione Bruno Kessler, INFN—National Institute for Nuclear Physics, and CNR—National Research Council. We acknowledge support by Provincia Autonoma di Trento.

S.N and E.T. contributed equally to this manuscript.

Appendix A: MNIST dataset

This section evaluates our proposed quantum neural network (QNN) architecture using the MNIST database of handwritten digits [49]. MNIST presents a significantly larger input feature space compared to the other real-world datasets discussed in Sec. III B. Specifically, each sample is a grayscale image comprising $28 \times 28 = 784$ pixels.

We performed binary classification for all unique digit pairs within the dataset. Our initial experiments, depicted in Fig. 6a, address the scenario where the complete 784-feature vector can be processed by a single product module (as defined in Eq. 7). This setup is analogous to the configurations discussed in Sec. III. The results show that all digit pairs can be classified with high accuracies on a test set exceeding 92%. Given the balanced nature of the dataset, the F1 scores are similar. The lowest classification performance was observed for the digit pairs 7-9 and 4-9. Furthermore, a slight improvement in accuracy was noted when increasing the number of product modules N . In contrast, increasing the number of factor modules k within each product module did not yield noticeable performance gains for this dataset.

Processing high-dimensional datasets like MNIST on current quantum hardware may necessitate partitioning the input features across multiple modules, a strategy proposed in Ref. [21] and briefly reviewed in Sec. II E. For the MNIST dataset, amplitude encoding the

entire feature vector into a quantum register would require 10 qubits. Such requirements can quickly encounter hardware limitations, for instance, with potential native SWAP test implementations on photonic [32–34] or trapped ions [35, 36] quantum computing platforms .

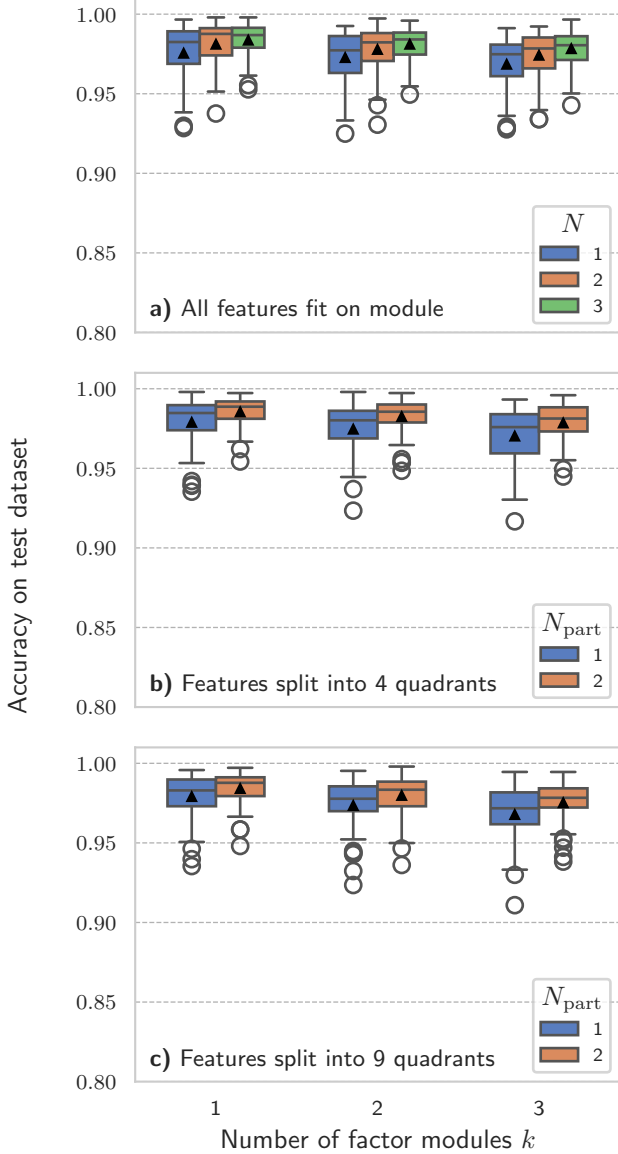


Figure 6. Accuracy results for binary classification after training our generalized QNN (Eq. 7) on the MNIST dataset. Each boxplot contains 45 data points corresponding to all possible combinations of digit pairs. In each case we considered a random subset of 10% of the full dataset (hyperparameters discussed in Sec. III A; early stopping using accuracy on validation set). **a)** Each of the N product modules gets the whole feature vector as input. **b)** **(c)** The feature vector is split into 4 (9) equal image quadrants (see also Sec. II E). Each quadrant is the input to N_{part} product modules, with k factor modules each.

To address this, we compare the results from the full-

feature configuration (Fig. 6a) with scenarios where the input features are divided into 4 (Fig. 6b) or 9 (Fig. 6c) equal, non-overlapping spatial partitions. Each partition corresponds to a distinct region of the original image. For example, with 4 partitions, the image is divided into four 14×14 sub-images (top-left, top-right, bottom-left, bottom-right). Similarly, 9 partitions correspond to nine 7×7 sub-images arranged in a grid.

In these partitioned configurations, each image partition is fed as input to N_{part} different product modules. Within each such product module, all k factor modules also receive this same input partition. Overall the network is then composed of $\# \text{Partitions} \times N_{\text{part}}$ product modules with k factor modules each.

For both scenarios with partitioned feature vectors we don’t observe a noticeable performance decrease in classification accuracy. Like in the case where the full feature vector fits onto a single module, we see a slightly improved performance when increasing the number of modules (N_{part}), while increasing the number of factor modules k has no significant effect.

To summarize, even when quantum hardware might not have enough qubits to encode large feature vectors into single modules, splitting the features onto multiple modules does not necessarily reduce performance when learning classical datasets. It remains an open question whether similar conclusions hold for learning quantum data.

Appendix B: Derivation of Eq. 13

In this Appendix we explicitly calculate

$$\sum_i (\mathbf{x}_i^\pm \cdot \mathbf{w}_j)^2 = 2^{d-1} \|\mathbf{w}_j\|^2, \quad (\text{B1})$$

which was used in deriving Eq. 14 in Sec. III C 1 and holds for $d > 2$. We also discuss the case $d = 2$ and show the necessary condition (analogous to Eq. 14) for learning the parity check in 2 dimensions.

To start, we can expand the above sum to

$$\sum_i (\mathbf{x}_i^\pm \cdot \mathbf{w}_j)^2 = \sum_i \left(\sum_{k=1}^d w_{j,k}^2 + \sum_{1 \leq m < n \leq d} 2x_{i,m}^\pm x_{i,n}^\pm w_{j,m} w_{j,n} \right). \quad (\text{B2})$$

Recall that the sum \sum_i goes over the 2^{d-1} different representative vectors with label $+1$ or -1 respectively. The first part of the expansion can thus be written as $\sum_i \|\mathbf{w}_j\|^2 = 2^{d-1} \|\mathbf{w}_j\|^2$. The second part of the expansion can be written as

Appendix C: Spiral datasets

$$\begin{aligned} & \sum_{1 \leq m < n \leq d} 2w_{j,m}w_{j,n} \sum_i x_{i,m}^\pm x_{i,n}^\pm \\ &= \sum_{1 \leq m < n \leq d} 2w_{j,m}w_{j,n} S^\pm(d), \end{aligned} \quad (\text{B3})$$

where the sum $S^\pm(d)$ does not depend on the indices m, n (due to symmetry) and only on the dimension d of the problem and the label of the representative vectors. For $d > 2$ the sum evaluates to

$$S^\pm(d > 2) = (+1)2^{d-2} + (-1)2^{d-2} = 0. \quad (\text{B4})$$

To see this, we can count for how many of the 2^{d-1} vectors, over which the sum \sum_i iterates, the product $x_{i,m}^\pm x_{i,n}^\pm$ has a positive or negative sign: There are two possibilities for the product to be $+1$, i.e. $x_{i,m}^\pm = x_{i,n}^\pm = \pm 1$. For either of the two possibilities, the remaining $d-2$ entries have to be even or odd respectively (depending on the label of \mathbf{x}^\pm), i.e. there are 2^{d-3} possible vectors. In total we thus have $2 \cdot 2^{d-3} = 2^{d-2}$ vectors in the sum \sum_i where $x_{i,m}^\pm x_{i,n}^\pm = +1$. The analogous argument then holds for $x_{i,m}^\pm x_{i,n}^\pm = -1$ and we get Eq. B4. The original sum in Eq. B3 thus also evaluates to zero and we obtain the necessary condition Eq. 13 for the network to learn the parity check in $d > 2$ dimensions.

For $d = 2$, the situation is different: Since there are only two entries in \mathbf{x}_i^\pm , the product $x_{i,m}^\pm x_{i,n}^\pm$ can only be positive for \mathbf{x}_i^+ , or only negative for \mathbf{x}_i^- . In either of the two cases we sum over the two possible vectors with the respective label and obtain

$$S^\pm(d = 2) = \pm 2. \quad (\text{B5})$$

For the original expansion we can thus write

$$\sum_i (\mathbf{x}_i^\pm \cdot \mathbf{w}_j)^2 = 2\|\mathbf{w}_j\|^2 \pm 4w_{j,1}w_{j,2}. \quad (\text{B6})$$

Using this expression in Eq. 12, we obtain the following necessary condition, which needs to be fulfilled for the neural network to be able to learn the parity check in two dimensions:

$$\sum_{j=1}^N \frac{c_j w_{j,1} w_{j,2}}{\|\mathbf{w}'_j\|^2} > 0. \quad (\text{B7})$$

This can be easily satisfied, as also confirmed by our numerical results in Sec. III C, e.g. by choosing $N = c_1 = w_{1,1} = w_{1,2} = 1$.

In this section we consider the binary n -spiral task, which is another classical synthetic dataset that poses a non-trivial learning challenge due to its complex non-linear decision boundaries [52]. Similar to the case of the parity check function (see Section III C 2), we find that the standard architecture (Eq. 6) is insufficient for learning higher-order instances of the dataset (all two-dimensional). However, utilizing our proposed architecture (see Sec. II D) with generalized SWAP tests, we find close to optimal performance when scaling up the network.

We generated a collection of binary n -spiral datasets with 1000 samples per class for spirals of order one, two and three, where the order denotes the number of times the spirals wind around the origin. In all three cases the generated data is two-dimensional. Specifically, we generate the feature vectors \mathbf{x}_i^\pm for the two classes $+1$ and -1 as follows:

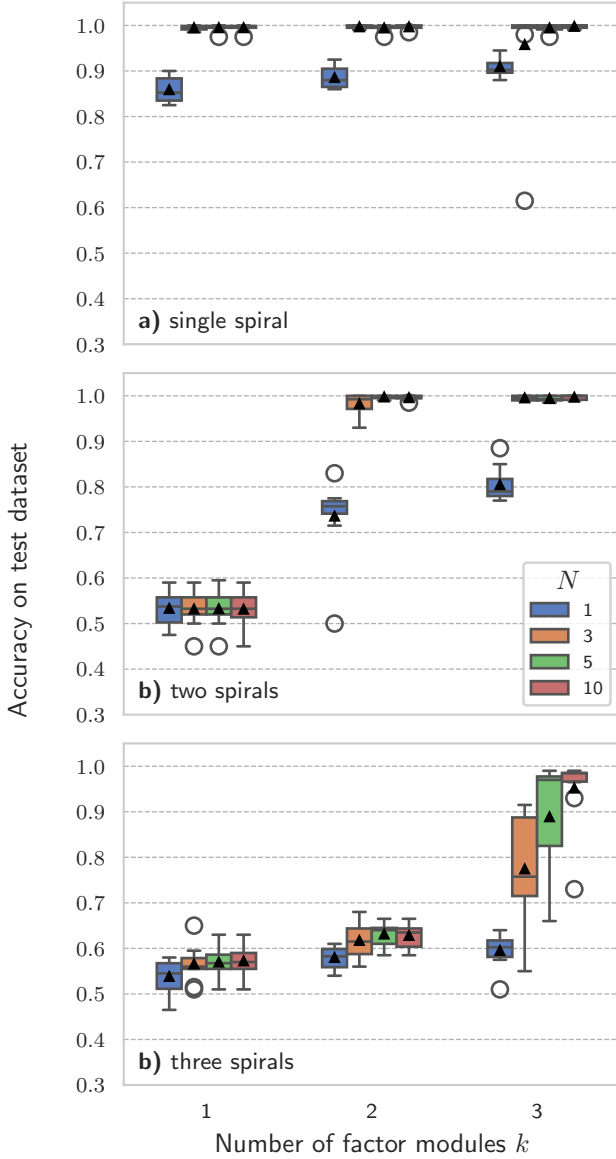
$$\mathbf{x}_i^\pm = \begin{pmatrix} \pm r_i \sin(\theta_i) + \epsilon_x \\ \pm r_i \cos(\theta_i) + \epsilon_y \end{pmatrix}, \quad (\text{C1})$$

where $r_i = 0.1 \cdot \theta_i$ defines the radius of the spiral, and $\theta_i = N_r \cdot 2\pi \cdot i/N$ is the angle for sample $i = 1, \dots, N_s$. The terms $\epsilon_x, \epsilon_y \sim \mathcal{N}(0, 0.025^2)$ represent Gaussian noise. Here, N_r indicates the spiral order and $N_s = 1000$ denotes the number of samples per class.

The feature vectors \mathbf{x}_i^\pm are then encoded into a quantum register using amplitude encoding. In contrast to all of the so far considered datasets, the magnitude of the feature vector encodes crucial information about the two classes for the n -spiral task. However, as our architecture is only able to process normalized input vectors (amplitude encoding considers only the angle information but loses the magnitude information due to its underlying quantum circuit, see Eq. 4), we have to encode the norm of the two-dimensional feature vectors into a third feature, so that our network effectively trains on a three-dimensional dataset. Therefore, in a quantum implementation for solving the spiral datasets, the data and weight registers would require two qubits each.

The accuracy results on a test dataset are shown in Figure 7, with all hyperparameters chosen as described in Sec. III A. As for the MNIST dataset, we considered early stopping on validation set accuracy as it is the chosen performance metric here. The architecture shows increased performance with a higher number of product modules N and factor modules k . Specifically, increasing the order of the dataset beyond one spiral, requires $k > 1$ to achieve meaningful prediction performance. Furthermore, increasing k alone is not enough, but has to be combined with an increased number of product modules N , similar to what we observed for the parity check function in Sec. III C.

For instance, we note that single round spirals (first order) are classified optimally with $N \geq 2$ and $k = 1$ (see Fig. 7a). However, for second and third order spirals



(Figs. 7b and 7c), we require $N \geq 3$, $k = 2$ and $N \geq 10$, $k = 3$ respectively.

Figure 7. Accuracy results on test datasets for the n -spiral tasks of order one, two and three (denoting the number of times the spirals wind around the origin). For increasing the number N of product modules and the number k of factor modules (see Eq. 7). Each boxplot contains 10 points, one for each fold. Horizontal lines represent the median and triangle markers indicate mean values.

[1] P. Wittek, *Quantum Machine Learning* (Elsevier, 2014).
 [2] S. Lloyd, M. Mohseni, and P. Rebentrost, Quantum algorithms for supervised and unsupervised machine learning (2013), arXiv:1307.0411 [quant-ph].
 [3] J. Biamonte, P. Wittek, N. Pancotti, P. Rebentrost, N. Wiebe, and S. Lloyd, *Nature* **549**, 195 (2017).
 [4] M. Schuld and F. Petruccione, *Machine Learning with Quantum Computers* (Springer International Publishing,

2021).
 [5] D. Pastorello, *Concise Guide to Quantum Machine Learning* (Springer Nature Singapore, 2023).
 [6] P. Rebentrost, M. Mohseni, and S. Lloyd, *Physical Review Letters* **113**, 130503 (2014).
 [7] M. Schuld, A. Bocharov, K. M. Svore, and N. Wiebe, *Physical Review A* **101**, 032308 (2020).
 [8] M. Cerezo, A. Arrasmith, R. Babbush, S. C. Benjamin,

- S. Endo, K. Fujii, J. R. McClean, K. Mitarai, X. Yuan, L. Cincio, and P. J. Coles, *Nature Reviews Physics* **3**, 625 (2021).
- [9] A. Peruzzo, J. McClean, P. Shadbolt, M.-H. Yung, X.-Q. Zhou, P. J. Love, A. Aspuru-Guzik, and J. L. O'Brien, *Nature Communications* **5**, 4213 (2014).
- [10] E. Farhi, J. Goldstone, and S. Gutmann, A quantum approximate optimization algorithm (2014), arXiv:1411.4028 [quant-ph].
- [11] L. Cincio, Y. Subaşı, A. T. Sornborger, and P. J. Coles, *New Journal of Physics* **20**, 113022 (2018).
- [12] A. G. Rattew, S. Hu, M. Pistoia, R. Chen, and S. Wood, A domain-agnostic, noise-resistant, hardware-efficient evolutionary variational quantum eigensolver (2020), arXiv:1910.09694 [quant-ph].
- [13] A. Kandala, A. Mezzacapo, K. Temme, M. Takita, M. Brink, J. M. Chow, and J. M. Gambetta, *Nature* **549**, 242 (2017).
- [14] F. Tacchino, C. Macchiavello, D. Gerace, and D. Bajoni, *npj Quantum Information* **5**, 10.1038/s41534-019-0140-4 (2019).
- [15] F. Tacchino, P. Barkoutsos, C. Macchiavello, I. Tavernelli, D. Gerace, and D. Bajoni, *Quantum Science and Technology* **5**, 044010 (2020).
- [16] J. R. McClean, S. Boixo, V. N. Smelyanskiy, R. Babbush, and H. Neven, *Nature Communications* **9**, 4812 (2018).
- [17] M. Cerezo, M. Larocca, D. García-Martín, N. L. Diaz, P. Braccia, E. Fontana, M. S. Rudolph, P. Bermejo, A. Ijaz, S. Thanasilp, E. R. Anschuetz, and Z. Holmes, Does provable absence of barren plateaus imply classical simulability? or, why we need to rethink variational quantum computing (2023).
- [18] M. Ragone, B. N. Bakalov, F. Sauvage, A. F. Kemper, C. Ortiz Marrero, M. Larocca, and M. Cerezo, *Nature Communications* **15**, 7172 (2024).
- [19] J. Zhao, Y.-H. Zhang, C.-P. Shao, Y.-C. Wu, G.-C. Guo, and G.-P. Guo, *Physical Review A* **100**, 012334 (2019).
- [20] P. Li and B. Wang, *Neural Networks* **130**, 152 (2020).
- [21] D. Pastorello and E. Blanzieri, *International Journal of Quantum Information* , 2450018 (2024).
- [22] H. Buhman, R. Cleve, J. Watrous, and R. de Wolf, *Physical Review Letters* **87**, 167902 (2001).
- [23] M. Schuld and F. Petruccione, *Supervised Learning with Quantum Computers*, Quantum Science and Technology (Springer International Publishing, Cham, 2018).
- [24] F. Arute, K. Arya, R. Babbush, D. Bacon, J. C. Bardin, R. Barends, R. Biswas, S. Boixo, F. G. S. L. Brandao, D. A. Buell, B. Burkett, Y. Chen, Z. Chen, B. Chiaro, R. Collins, W. Courtney, A. Dunsworth, E. Farhi, B. Foxen, A. Fowler, C. Gidney, M. Giustina, R. Graff, K. Guerin, S. Habegger, M. P. Harrigan, M. J. Hartmann, A. Ho, M. Hoffmann, T. Huang, T. S. Humble, S. V. Isakov, E. Jeffrey, Z. Jiang, D. Kafri, K. Kechedzhi, J. Kelly, P. V. Klimov, S. Knysh, A. Korotkov, F. Kostritsa, D. Landhuis, M. Lindmark, E. Lucero, D. Lyakh, S. Mandrà, J. R. McClean, M. McEwen, A. Megrant, X. Mi, K. Michielsen, M. Mohseni, J. Mutus, O. Naaman, M. Neeley, C. Neill, M. Y. Niu, E. Ostby, A. Petukhov, J. C. Platt, C. Quintana, E. G. Rieffel, P. Roushan, N. C. Rubin, D. Sank, K. J. Satzinger, V. Smelyanskiy, K. J. Sung, M. D. Trevithick, A. Vainsencher, B. Villalonga, T. White, Z. J. Yao, P. Yeh, A. Zalcman, H. Neven, and J. M. Martinis, *Nature* **574**, 505 (2019).
- [25] S. Bravyi, A. W. Cross, J. M. Gambetta, D. Maslov, P. Rall, and T. J. Yoder, *Nature* **627**, 778 (2024).
- [26] C. Piltz, T. Sriarunothai, S. S. Ivanov, S. Wölk, and C. Wunderlich, *Science Advances* **2**, 10.1126/sciadv.1600093 (2016).
- [27] J.-S. Chen, E. Nielsen, M. Ebert, V. Inlek, K. Wright, V. Chaplin, A. Maksymov, E. Pérez, A. Poudel, P. Maunz, and J. Gamble, *Quantum* **8**, 1516 (2024).
- [28] M. Liu, R. Shaydulin, P. Niroula, M. DeCross, S.-H. Hung, W. Y. Kon, E. Cervero-Martín, K. Chakraborty, O. Amer, S. Aaronson, A. Acharya, Y. Alexeev, K. J. Berg, S. Chakrabarti, F. J. Curchod, J. M. Dreiling, N. Erickson, C. Foltz, M. Foss-Feig, D. Hayes, T. S. Humble, N. Kumar, J. Larson, D. Lykov, M. Mills, S. A. Moses, B. Neyenhuis, S. Eloul, P. Siegfried, J. Walker, C. Lim, and M. Pistoia, *Nature* **640**, 343 (2025).
- [29] M. Meth, J. Zhang, J. F. Haase, C. Edmunds, L. Postler, A. J. Jena, A. Steiner, L. Dellantonio, R. Blatt, P. Zoller, T. Monz, P. Schindler, C. Muschik, and M. Ringbauer, *Nature Physics* **21**, 570 (2025).
- [30] L. Brodoloni, J. Vovrosh, S. Julià-Farré, A. Dauphin, and S. Pilati, Spin-glass quantum phase transition in amorphous arrays of rydberg atoms (2025).
- [31] D. González-Cuadra, M. Hamdan, T. V. Zache, B. Braverman, M. Kornjača, A. Lukin, S. H. Cantú, F. Liu, S.-T. Wang, A. Keesling, M. D. Lukin, P. Zoller, and A. Bylinskii, *Nature* **642**, 321 (2025).
- [32] M. Fiorentino, T. Kim, and F. N. C. Wong, *Physical Review A* **72**, 012318 (2005).
- [33] M.-S. Kang, J. Heo, S.-G. Choi, S. Moon, and S.-W. Han, *Scientific Reports* **9**, 10.1038/s41598-019-42662-4 (2019).
- [34] A. Baldazzi, N. Leone, M. Sanna, S. Azzini, and L. Pavesi, *Quantum Science and Technology* **9**, 045053 (2024).
- [35] N. M. Linke, S. Johri, C. Figgatt, K. A. Landsman, A. Y. Matsuura, and C. Monroe, *Physical Review A* **98**, 052334 (2018).
- [36] C.-H. Nguyen, K.-W. Tseng, G. Maslennikov, H. C. J. Gan, and D. Matsukevich, Experimental swap test of infinite dimensional quantum states (2021).
- [37] K. Hornik, M. Stinchcombe, and H. White, *Neural Networks* **2**, 359 (1989).
- [38] K. Hornik, *Neural Networks* **4**, 251 (1991).
- [39] R. Livni, S. Shalev-Shwartz, and O. Shamir, in *Proceedings of the 28th International Conference on Neural Information Processing Systems - Volume 1, NIPS'14*, Vol. 1 (MIT Press, Cambridge, MA, USA, 2014) pp. 855–863.
- [40] M. Blondel, M. Ishihata, A. Fujino, and N. Ueda, in *Proceedings of The 33rd International Conference on Machine Learning* (PMLR, 2016) pp. 850–858.
- [41] Y. Shin and J. Ghosh, in *IJCNN-91-Seattle International Joint Conference on Neural Networks*, Vol. i (1991) pp. 13–18 vol.1.
- [42] C.-K. Li, *Neural Processing Letters* **17**, 1 (2003).
- [43] S. S. Mannelli, E. Vanden-Eijnden, and L. Zdeborová, Optimization and Generalization of Shallow Neural Networks with Quadratic Activation Functions (2020), arXiv:2006.15459 [cs].
- [44] C. Luo, J. Zhan, L. Wang, and Q. Yang, Cosine normalization: Using cosine similarity instead of dot product in neural networks (2017).
- [45] A. Pinkus, *Acta Numerica* **8**, 143 (1999).
- [46] P. Huber, J. Haber, P. Barthel, J. J. García-Ripoll,

- E. Torrontegui, and C. Wunderlich, Realization of a quantum perceptron gate with trapped ions (2021).
- [47] Y.-H. Luo and S.-Y. Shen, *IEEE Transactions on Neural Networks* **11**, 1485 (2000).
- [48] J. Long, W. Wu, and D. Nan, in *Advances in Neural Networks – ISNN 2007*, edited by D. Liu, S. Fei, Z.-G. Hou, H. Zhang, and C. Sun (Springer, Berlin, Heidelberg, 2007) pp. 1110–1116.
- [49] Y. Lecun, L. Bottou, Y. Bengio, and P. Haffner, *Proceedings of the IEEE* **86**, 2278 (1998).
- [50] M. Kelly, R. Longjohn, and K. Nottingham, Home - UCI Machine Learning Repository, <https://archive.ics.uci.edu/> (2024).
- [51] LIBSVM Data: Classification (Binary Class), <https://www.csie.ntu.edu.tw/~cjlin/libsvmtools/datasets/binary.html>.
- [52] V. Dhar, A. Tickoo, R. Koul, and B. Dubey, *Pramana* **74**, 307 (2010).
- [53] C. Mingard, J. Pointing, C. London, Y. Nam, and A. A. Louis, Exploiting the equivalence between quantum neural networks and perceptrons (2024).
- [54] A. Javadi-Abhari, M. Treinish, K. Krsulich, C. J. Wood, J. Lishman, J. Gacon, S. Martiel, P. D. Nation, L. S. Bishop, A. W. Cross, B. R. Johnson, and J. M. Gambetta, Quantum computing with Qiskit (2024), arXiv:2405.08810.
- [55] S. A. Wilkinson and M. J. Hartmann, Evaluating the performance of sigmoid quantum perceptrons in quantum neural networks (2022), arXiv:2208.06198 [quant-ph].